J. Fluid Mech. (1989), *vol.* 206, *pp.* 517–544
Printed in Great Britain

Numerical simulations of multiple flow transitions in axisymmetric annulus convection

By P. LE QUÉRÉ[1] AND J. PÉCHEUX[2]
[1] LIMSI-CNRS, BP 30, 91406 Orsay Cedex, France
[2] LEA-UA CNRS 191, 40 Av. Recteur Pineau, 86022 Poitiers Cedex, France

(Received 8 May 1988 and in revised form 14 March 1989)

We examine numerically the behaviour of the solutions of the axisymmetric Boussinesq equations in a tall, differentially heated, air-filled annulus. The numerical algorithm integrates the time-dependent equations in primitive variables and combines a pseudospectral Chebyshev spatial expansion with a second-order time-stepping scheme. The instability of the conduction regime is found to be unsteady cross-rolls. By assuming Hopf bifurcation, we can accurately determine the critical Rayleigh number. As the Rayleigh number increases, the solution is monoperiodic at first. Then it undergoes a period-doubling bifurcation. When the Rayleigh number is further increased, the solution reverts to a monocellular steady state through subcritical bifurcations with hysteresis. At even higher Rayleigh number, boundary-layer instability sets in, in the form of travelling waves. This instability has the characteristics of a supercritical Hopf bifurcation. We examine the space–time structure of the two types of unsteady solutions. We have presented the basic periods of the steady oscillations as functions of the Rayleigh number in the vicinity of the Hopf bifurcation points, and have also computed the Nusselt numbers for the various flow regimes.

1. Introduction

We consider an air-filled tall vertical annulus in a gravitational field. The inner and outer walls are kept at two different constant temperatures and the top and bottom walls are thermally insulated. Natural convection in cylindrical cavities has not been studied in as much detail as in Cartesian geometry, yet it has many applications in thermal engineering and in the insulation of nuclear reactors. It also presents important examples of bifurcation in fluid dynamics. In Cartesian coordinates the two-dimensional Boussinesq equations depend on three dimensionless parameters: the Rayleigh number Ra, the Prandtl number Pr and the aspect ratio A, defined as the ratio of the height of the cavity to its width. The annulus configuration requires an additional fourth dimensionless parameter, the radius ratio η, defined as the ratio of the inner radius to the outer radius of the annulus ($0 < \eta < 1$). In a tall annulus, for small Rayleigh numbers, the flow and the isotherms are parallel to the vertical walls, except in the vicinity of the top and bottom ends. These features are accurately represented by the one-dimensional analytical solution found in an annulus of infinite length. The linear stability analysis of the latter solution was undertaken by Choi & Korpela (1980). The principal finding is that, for fluids of moderate Prandtl number, the conduction regime becomes unstable to unsteady perturbations in the form of cross-rolls, the so called 'cat's eye' instability. These perturbations propagate upwards when the inner cylinder is warmer than the outer one and reach

their maximum amplitude in the middle of the slot. This differs significantly from the corresponding instability in Cartesian geometry which takes the form of stationary disturbances, as a consequence of the skew-symmetry of the base flow and temperature profiles. This can only be true for an ideal Boussinesq fluid. Lauriat & Desrayaud (1985*a*) have shown that taking radiative effects into account in a Cartesian geometry breaks the skew-symmetry of the profiles and results in unsteady perturbations. The choice of basis functions made by Choi & Korpela did not allow them to cover the whole range of Prandtl numbers and radius ratios. More recently, by using Bessel functions, Shaaban & Osizik (1982) have obtained complementary results. However, there is still a range of Prandtl numbers and radius ratios for which reliable results are lacking: this is probably due to a fundamental change in the nature of the instability when varying the radius ratio.

These linear stability analyses assumed axisymmetric perturbations. The validity of this assumption was recently addressed by McFadden *et al.* (1984) who investigated the stability of the conduction regime for both axisymmetric disturbances and disturbances of wavenumber one in the azimuthal direction. They have shown that the latter mode is more unstable than the former when the radius ratio is less than 0.44 for a Prandtl number of 0.71. This agrees with the experimental results obtained by Choi & Korpela (1980) who report on the existence of axisymmetric disturbances in a cavity of radius ratio equal to 0.68. Azimuthal structures were found in the experiments of Weidman & Mehrdadtehranfar (1985) who studied a fluid of moderately large Prandtl number in a very tall annulus.

Few full Navier–Stokes computations have been performed in the vertical annulus configuration. De Vahl Davis & Thomas (1969) and Thomas & de Vahl Davis (1970) were the first to investigate the vertical differentially heated annulus. These pioneering computations were done in annuli of aspect ratio between 5 and 15, limited to relatively low Rayleigh-number values, given the available computer resources of the time. More recently, Lee, Korpela & Horne (1982) investigated the instability of the conduction regime in tall annuli of aspect ratio ranging from 10 to 20 for various Prandtl-number fluids. Their numerical scheme is of finite-difference type and integrates the unsteady Boussinesq equations in stream function–vorticity formulation. Unsteady solutions are found for Rayleigh-number values that are in good agreement with the linear stability results. Lee & Korpela (1983) have conducted more extensive calculations in tall Cartesian cavities. They have tried to reach the unsteady regime resulting from the instability of the boundary layers for a fluid corresponding to water. At a high Rayleigh number, their results show travelling waves propagating in the boundary layers but they do not seem to have integrated long enough in time to reach the asymptotic unsteady solution. There has recently been a revival of interest in the vertical annulus configuration: see, for example, the experimental results by Prasad & Kulacki (1985) and the numerical computations by Lin & Nansteel (1987) for water near the density maximum.

The aim of this work is to study the sequence of events that take place in a tall air-filled annulus as the Rayleigh number is progressively increased from zero to the bifurcation corresponding to the onset of travelling waves. Most of the computations are performed in a cavity of aspect ratio equal to 16 and for a radius ratio equal to 0.8. In the next section, we recall the governing equations and describe the numerical algorithm used to integrate the time-dependent equations. In §3 we consider base flow solutions belonging to the conduction regime; we deal with the boundary-layer regime in §4. In the last section we present local and global Nusselt numbers for the various flow regimes.

2. Governing equations and numerical scheme

2.1. *Governing equations*

Consider the flow of a Newtonian fluid of volumetric expansion coefficient β in a closed annulus of height $2H$ extending from $-H$ to H in the z-direction and from R_1 to R_2 in the r-direction. The positive z-direction of the cylindrical coordinate system is chosen opposite to the gravity vector of modulus g. The inner and outer cylinders are maintained at different uniform temperatures T_1 and T_2 (generally $\Delta T = T_1 - T_2 > 0$) while the top and bottom walls are thermally insulating. We assume that the fluid satisfies the Boussinesq approximation and we consider sufficiently large values of the radius ratio so that, following the results obtained by McFadden *et al.* (1984), the flow is likely to be axisymmetric.

We introduce

$$L_{\text{ref}} = H, \quad V_{\text{ref}} = (g\beta\Delta T H)^{\frac{1}{2}}, \quad t_{\text{ref}} = \left(\frac{H}{g\beta\Delta T}\right)^{\frac{1}{2}}$$

as reference quantities for length, velocity and time. Defining the dimensionless temperature as $\Theta = (T - T_r)/(T_2 - T_1)$ with $T_r = \frac{1}{2}(T_1 + T_2)$, the governing equations can then be cast in the following non-dimensional forms:

$$\frac{\partial u}{\partial r} + \frac{u}{r} + \frac{\partial w}{\partial z} = 0, \tag{1}$$

$$\frac{\partial u}{\partial t} + u\frac{\partial u}{\partial r} + w\frac{\partial u}{\partial z} = -\frac{\partial P}{\partial r} + \frac{1}{Gr_H^{\frac{1}{2}}}\left(\nabla^2 u - \frac{u}{r^2}\right), \tag{2}$$

$$\frac{\partial w}{\partial t} + u\frac{\partial w}{\partial r} + w\frac{\partial w}{\partial z} = -\frac{\partial P}{\partial z} + \frac{1}{Gr_H^{\frac{1}{2}}}\nabla^2 w + \Theta, \tag{3}$$

$$\frac{\partial \Theta}{\partial t} + u\frac{\partial \Theta}{\partial r} + w\frac{\partial \Theta}{\partial z} = \frac{1}{Pr\, Gr_H^{\frac{1}{2}}}\nabla^2 \Theta, \tag{4}$$

where t is the time, u and w are the velocity components in the r-(horizontal) and z-directions respectively and P the deviation from the hydrostatic pressure divided by the mean density multiplied by V_{ref}^2. In these equations, ∇^2 is the cylindrical Laplacian operator

$$\left(\frac{\partial^2}{\partial r^2} + \frac{1}{r}\frac{\partial}{\partial r} + \frac{\partial^2}{\partial z^2}\right).$$

Gr_H is the Grashof number based on H ($= g\beta H^3 \Delta T/\nu^2$) and Pr ($= \nu/\kappa$) is the Prandtl number, where ν and κ are respectively the kinematic and thermal diffusivities of the fluid. The Rayleigh number Ra_H is equal to $Pr\, Gr_H$. In all the numerical computations, Pr will be set to 0.71.

In dimensionless coordinates the computational domain extends from $r_1 = R_1/H$ to $r_2 = R_2/H$ in the r-direction and from -1 to $+1$ in the z-direction. The aspect ratio A is thus equal to $2/(r_2 - r_1)$. The dynamic boundary conditions are the no-slip condition on all four walls of the cavity. The scaled temperature is respectively 0.5 and -0.5 on r_1 and r_2 if the inner wall is heated. On the horizontal walls $z = -1$ and $+1$, the adiabaticity boundary condition reads $\partial\Theta/\partial z = 0$.

2.2. *Numerical algorithm*

The numerical algorithm integrates the time-dependent equations (1)–(4) in primitive variables. It is an extension of the algorithm developed by Le Quéré & Alziary de Roquefort (1982, 1985*a*) in a Cartesian geometry.

The space discretization relies on spectral spatial expansions of the dependent variables in double truncated series of Chebyshev polynomials: any two-dimensional field $f(r,z,t)$ (where f stands for either u, w, P or Θ) is thus expanded as

$$f(r,z,t) = \sum_{n=0}^{N} \sum_{m=0}^{M} f_{nm}(t)\, T_n(\zeta)\, T_m(z), \tag{5}$$

where ζ is defined as $(2r-(r_1+r_2))/(r_2-r_1)$. The spectral coefficients f_{nm} are obtained by collocation at the Gauss–Lobatto Chebyshev points using the orthogonality relationships for the discrete cosine series:

$$f_{nm}(t) = \frac{4}{\bar{c}_n \bar{c}_m NM} \sum_{i=0}^{N} \sum_{j=0}^{M} \frac{1}{\bar{c}_i \bar{c}_j} f(\zeta_i, z_j, t)\, T_n(\zeta_i)\, T_m(z_j), \tag{6}$$

with $\zeta_i = \cos(i\pi/N)$, $i = 0,\ldots,N$; $z_j = \cos(j\pi/M)$, $j = 0,\ldots,M$; $\bar{c}_0 = \bar{c}_N = 2$, $\bar{c}_n = 1, 0 < n < N$. The time-stepping scheme is of finite-difference type. For stability considerations (Gottlieb & Orszag 1977), it is compulsory to resort to an implicit or semi-implicit treatment of the diffusive or viscous terms, while the nonlinear terms are generally treated explicitly. A second-order scheme which is generally used is the classical Adams–Bashforth/Crank–Nicolson scheme. More recently Vanel, Peyret & Bontoux (1986) have proposed another second-order scheme which combines a second-order backward Euler scheme with an Adams–Bashforth extrapolation of the nonlinear terms. These scheme possesses better stability properties when used in conjunction with the influence matrix technique to maintain the incompressibility condition. This property was demonstrated by Ehrenstein (1986) when the equations are formulated in stream-function and vorticity variables. Numerical experiments indicate that this property seems to carry over to the primitive variable formulation. When applied to a scalar advection–diffusion equation such as

$$\frac{\partial f}{\partial t} + \boldsymbol{V}\cdot\boldsymbol{\nabla} f = \nabla^2 f,$$

the scheme proposed by Vanel *et al.* (1986) reads

$$\frac{3f^{n+1} - 4f^n + f^{n-1}}{2\Delta t} + 2\boldsymbol{V}\cdot\boldsymbol{\nabla} f^n - \boldsymbol{V}\cdot\boldsymbol{\nabla} f^{n-1} = \nabla^2 f^{n+1}, \tag{7}$$

where Δt is the time step. This equation can be cast in an Helmholtz equation for the unknown field f at time $n+1$:

$$\nabla^2 f^{n+1} - \lambda f^{n+1} = -S_f, \tag{8}$$

where $\lambda = 3/2\Delta t$. The source term S_f of this equation comprises all the known quantities at previous time levels $n\Delta t$ and $(n-1)\,\Delta t$. In particular the nonlinear terms are classically evaluated pseudospectrally. The Helmholtz equation is then solved in the spectral space using the tau-method and an algorithm derived from the partial diagonalization algorithm proposed by Haidvogel & Zang (1979) for the Cartesian case. This algorithm relies on the expansion of the solution on a modified basis function which is the tensor product of the Chebyshev polynomials in one direction

with the eigenfunctions of the operator corresponding to the other direction. Since the symmetric role of the two space Cartesian variables is broken in cylindrical coordinates, one has to make a choice concerning the direction of the eigenfunction expansion. Examination of the asymptotic operation count shows that it is preferable to diagonalize the operator corresponding to the radial direction since this allows retention of the quasi-tridiagonal form of the $\partial^2/\partial z^2$ operator. Two sets of eigenvalues and eigenfunctions corresponding respectively to

$$\left(\frac{\partial^2}{\partial r^2}+\frac{1}{r}\frac{\partial}{\partial r}\right), \quad \left(\frac{\partial^2}{\partial r^2}+\frac{1}{r}\frac{\partial}{\partial r}-\frac{1}{r^2}\right)$$

have then to be computed in order to account for the different forms of the diffusion operators for the u-velocity component and for the other variables. All the eigenvalues and eigenfunctions computed for various values of the radius ratio and for values of N up to 32 were found to be real. (This property lacks theoretical proof.) Finally all the terms specific to the cylindrical coordinates such as multiplication by r or $1/r$ were computed spectrally. For instance, evaluation of the spectral coefficients of f/r given the spectral coefficients of f requires the inversion of a tridiagonal matrix system.

The incompressibility constraint is maintained through the use of the influence matrix technique which was introduced by Kleiser & Schumann (1980) for the one-dimensional Chebyshev case. We refer to Le Quéré & Alziary de Roquefort (1985*a*) for the details of the algorithm in the two-dimensional Chebyshev case. The efficiency of the influence matrix algorithm lies in the fact that at each time step, a velocity field that possesses a zero-divergence at the boundary of the computational domain is obtained in only one iteration. This velocity field is not, however, exactly divergence-free within the computational domain owing to the non-commutativity of the tau-projection with the partial differentiation operators (see Haldenwang 1984). Care was taken to choose sufficiently high resolution to maintain the Euclidian norm of the divergence of the velocity field at less than 5×10^{-4} throughout the computations.

For the purpose of easier comparison with earlier work, some of the result will be presented in different dimensionless units than those used to perform the actual integration. In particular the discussion of the results below is made in terms of the Rayleigh number, Ra, based on the cavity width (r_2-r_1) as reference length ($Ra = 8Ra_H/A^3$). For the sake of clarity all the drawings are presented in a cavity of aspect ratio equal to 12.

3. The conduction regime

3.1. *The steady conduction regime*

When the equations are integrated for low values of the Rayleigh number (typically less than 6×10^3), the numerical solutions evolve rapidly towards a steady state. For instance, when the equations are integrated with a Rayleigh-number value set to 4×10^3 starting from rest, the solution reaches a steady state at non-dimensional time equal to 10. The corresponding flow is the well-known conduction regime with isotherms parallel to the isothermal vertical boundaries and a parallel flow extending over more than 90% of the cavity height.

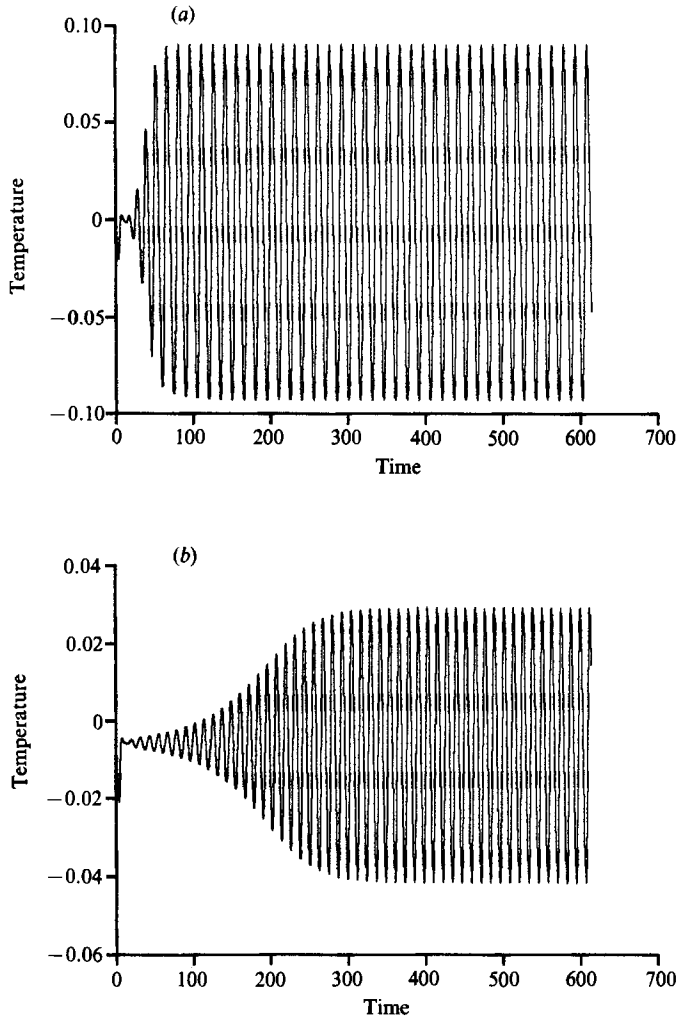

FIGURE 1. Time evolution of the temperature at point $\zeta = 0$, $z = 0.26$; (*a*) $Ra = 8 \times 10^3$, (*b*) $Ra = 7 \times 10^3$; $A = 16$, $\eta = 0.8$; $N = 24$, $M = 72$.

3.2. *Unsteady motion*

3.2.1. *Structure of unsteady motion*

When the equations are integrated from rest with a value of the Rayleigh number set to 8×10^3, the numerical algorithm gives an asymptotic solution which is unsteady, periodic in time and shows fluctuations of constant amplitude, as shown in figure 1 (*a*). If integration is carried out with a smaller Ra value of 7×10^3 starting from the same initial condition (i.e. rest), one also obtains an asymptotic solution which is periodic in time and shows fluctuations of constant, albeit smaller, amplitude (figure 1*b*). The major difference with the previous case is that it takes much longer for the solution to reach its asymptotic state. The phase of exponential growth of the fluctuations is clearly visible on the figure. It is followed by a phase where nonlinear interactions take over and eventually saturate the amplitude of the fluctuations, leading to the asymptotic state of constant-amplitude fluctuations.

These time integrations were performed with a spatial resolution ($N = 24$, $M = 72$) and with a time step equal to 0.03. In order to check the accuracy of these solutions, the integration corresponding to an Ra value of 7×10^3 was repeated with an increased spatial resolution ($N = 32, M = 96$) and a smaller time step of 0.025. This allowed us to have a Chebyshev collocation point at the same physical location as the sampling point chosen for the coarser resolution. The time traces of the temperature at the sampling points virtually cannot be distinguished (differences less than 1×10^{-4}) which proves the adequacy of the coarser ($N = 24$, $M = 72$) resolution.

Once the asymptotic periodic solution is reached, it is possible to determine its mean time value from simple arithmetic averaging of the fields sampled over one or several periods of oscillations. Figure 2 presents time sequences of the fluctuating temperature and stream-function fields over one period of oscillation. These plots show that the fluctuations reach their maximum amplitude in the centre of the cavity just above mid-height. These fluctuations originate in the bottom part of the cavity. As they slowly drift upwards they grow in amplitude till mid-height of the cavity. Afterwards their amplitude slowly decreases and by the time they reach the uppermost part of the cavity, their amplitude has become almost zero. These structures should be compared to the eigenfunctions calculated by Hart (1971) for the linear instability of the flow in a differentially heated Cartesian slot in the conduction regime. One also sees that these structures are characterized by a wavelength that remains approximately constant as they proceed upwards and they consequently travel at a constant wave speed. Graphical evaluation of the wavelength at the location of maximum amplitude (just above mid-height of the cavity) yields $2.07(r_2 - r_1) \pm 2\%$ which corresponds to a wavenumber of 3.03. The period Π of the oscillations is 12.3 in units of $(H/g\beta\Delta T)^{0.5}$ which indicates that roughly 400 time steps are needed to integrate the equations over one time period. In the units used by Choi & Korpela this corresponds to a wave speed equal to 6.0×10^{-4}. The critical wavelength and wave speed found by Choi & Korpela in the infinitely long annulus for the same value of the radius ratio and of the Prandtl number are respectively $2.24(r_2 - r_1)$ and 7.0×10^{-4}.

3.2.2. *Accurate determination of the critical parameters*

Brute-force integration of the time-dependent equations can only provide upper and lower bounds of the critical Rayleigh number value. In order to obtain a more accurate determination of this critical value one has to assume the nature of the bifurcation that corresponds to the onset of unsteadiness. A reasonable assumption in view of the very small amplitude of the oscillations obtained for the value of Ra set to 7×10^3 is that loss of stability is due to the presence of a supercritical Hopf bifurcation in the continuous equations.

Three main consequences derive from this assumption (see e.g. Iooss 1972): the period of the oscillations tends continuously to the period of the oscillations at the Hopf bifurcation point; the correlation time, i.e. the time needed to reach the asymptotic solution, diverges as $(Ra - Ra_c)^{-1}$; the amplitude of the limit cycle behaves like $(Ra - Ra_c)^{0.5}$ in an interval around Ra_c^+. The latter feature can be used to determine the accurate location of the critical value. This requires the computation of several asymptotic solutions. One then has to determine a range of values of the Rayleigh number over which the squared amplitude of the oscillations behaves linearly with Ra. Extrapolation of this relationship to zero amplitude then gives an accurate determination of the critical value. We have chosen to look at the fluctuations of local and global quantities. The local quantities are the temperature

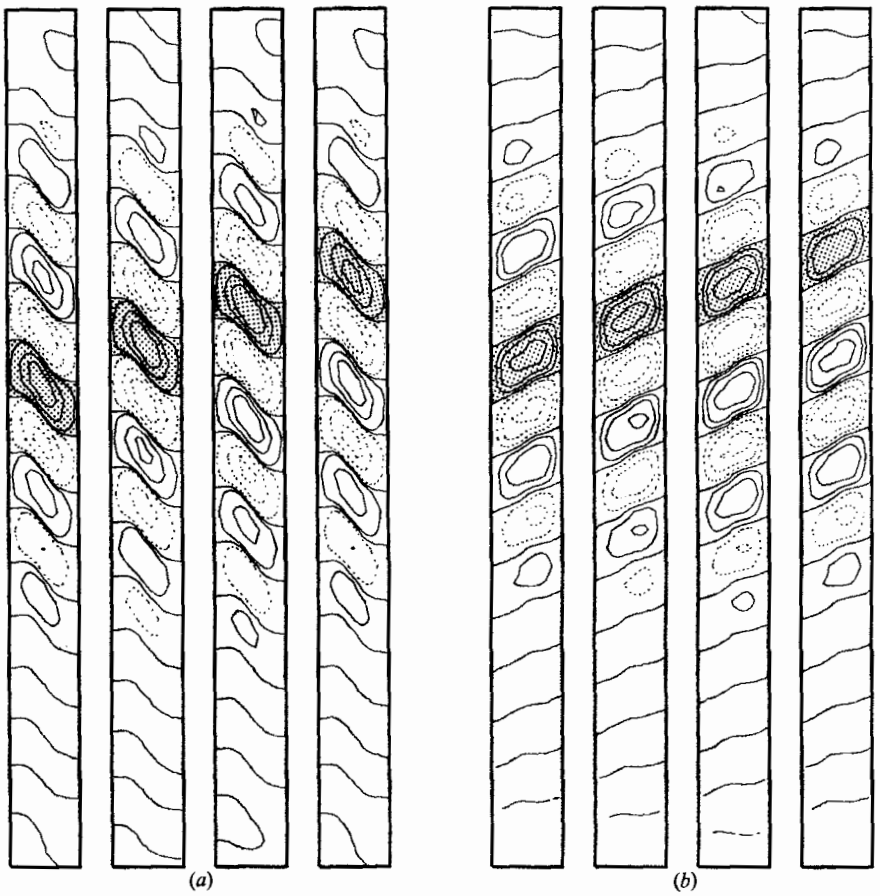

FIGURE 2. Time sequence of fluctuating temperature field (*a*) and of fluctuating stream function field (*b*), $Ra = 7 \times 10^3$; $A = 16$, $\eta = 0.8$; $N = 24$, $M = 72$. Time interval is 4.11. Temperature isovalues are 0, ± 0.002, ± 0.01, ± 0.02. Stream-function isovalues are 0, ± 0.00004, ± 0.0001, ± 0.0002. (maximum stream function is 0.0063). Negative isovalues are shown as dotted lines. One structure is shaded in grey so that its motion can be followed.

and w-velocity component at the monitoring point; a global quantity $E(\Theta)$ is defined as

$$E(\Theta) = \sum_{n,m} \Theta_{nm}^2,$$

where the Θ_{nm} are the spectral coefficients of the temperature field. Figure 3 shows the squared amplitudes of the fluctuations of these three quantities for four values of the Rayleigh number, 6900, 6950, 7000 and 7100. It can be seen that the squared amplitudes grow linearly with Ra in this range of Ra-values. Extrapolation of the relationships to zero provides an estimate of the accurate value, which turns out to be 6850 ± 10. The critical value found by Choi & Korpela in the annulus of infinite aspect ratio is 5770. In order to see if this difference between the two critical values was due to inaccuracy of our results or to finite-aspect ratio effects, we carried out determination of the critical value for annuli of aspect ratio equal to 20 and 25. The critical values found using the same methodology are respectively 6185 and 5965, showing that finite-aspect-ratio effects have a significant stabilizing influence on the

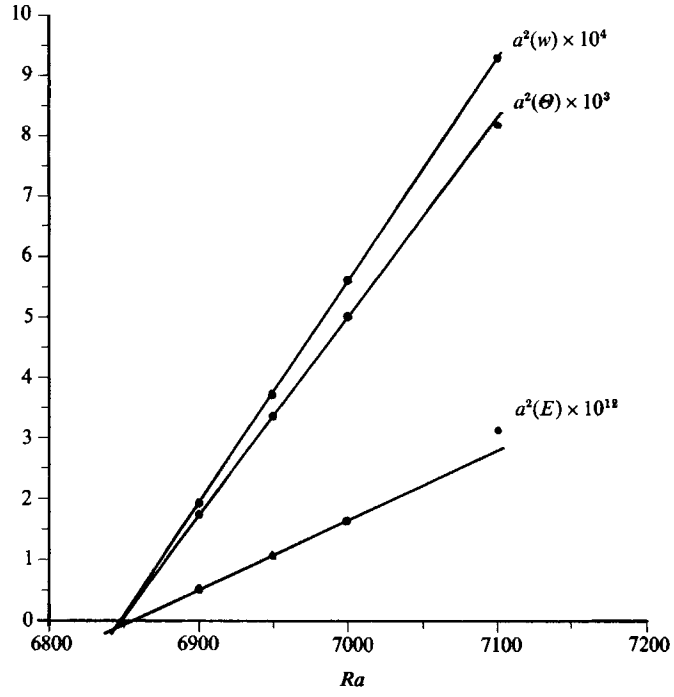

FIGURE 3. Evolution of the squared amplitudes of temperature $a^2(\Theta)$, of the w-velocity component $a^2(w)$ and of $a^2(E)$ as a function of Ra; $A = 16$, $\eta = 0.8$. Location of monitoring point: $\zeta = 0$, $z = 0.26$.

critical value corresponding to the transition to unsteady flow. The origin of this stabilizing effect is probably due to the vertical stratification which is known to delay the onset of transition (Bergholz 1978). The vertical stratification appears near the end regions and its relative penetration length increases with decreasing aspect ratio. The computations for $A = 20$ were carried out with $N = 24$, $M = 90$ and $\Delta t = 0.025$, and those for $A = 25$ with $N = 24$, $M = 96$ and $\Delta t = 0.03$.

3.2.3. *Evolution of the period of the oscillations*

The first consequence of the assumption of Hopf's bifurcation listed in the previous paragraph states that one can find a relationship between the dimensionless periods Π of the oscillations and the Rayleigh number in the vicinity of the Hopf bifurcation point. For the three aspect ratios considered and corresponding Ra values, these periods were carefully determined by noting the indices n where the product $(\Theta(n)-\Theta(n-1))(\Theta(n-1)-\Theta(n-2))$ at the monitoring point is negative during the course of integration. This measurement is independent of the location of the sampling point since all quantities at the interior points oscillate at the same frequency, modulo a phase lag. Table 1 shows for instance, the actual periods of the oscillations for the $A = 16$ case measured for four Rayleigh number values and also for Ra equal to 6850 for which we could not conclude on the nature of the asymptotic solution but could nonetheless accurately measure the period of the oscillations. For each value of the aspect ratio, a power-law relationship of the form $\Pi = \Pi(Ra_c)Ra^m$ was then established. The m exponent was found to decrease with increasing aspect ratio. Mean-square fits give $m = 0.67$ for $A = 25$, $m = 1.0$ for $A = 20$ and $m = 1.75$ for $A = 16$.

Ra	Π	$\Pi Ra^{-1.75}$
6850	11.838	2.2952×10^{-6}
6900	11.985	2.2943×10^{-6}
6950	12.141	2.2950×10^{-6}
7000	12.294	2.2949×10^{-6}
7100	12.60	2.2944×10^{-6}

TABLE 1. Evolution of the period Π of oscillations for $A = 16$; $\eta = 0.8$

For a given aspect ratio, the fact that the non-dimensional period behaves like Ra^m indicates that the dimensional period evolves like $H^{3m+\frac{1}{2}}\Delta T^{m-\frac{1}{2}}$. The dimensional period of the oscillations is thus an increasing function of the temperature difference since m is larger than $\frac{1}{2}$ for the three values of the aspect ratio. In a given experimental set-up, increasing the temperature difference slows down the upward drift of the cat's eyes. We have no definite explanation for this peculiar behaviour, which might be due to a stabilizing influence from the small vertical stratification that develops in finite aspect-ratio cavities. In order to make useful comparisons, it would be interesting to know the behaviour of the period of oscillations at criticality for the slot of infinite vertical extension. This dependence is unfortunately not available at the present time.

Table 2 shows the evolution of the critical Rayleigh number, wavelength λ_c and wave speed α_c for the three values of the aspect ratio and for the slot of infinite extension taken from the linear stability results by Choi & Korpela. The critical wave speeds were obtained by extrapolation of the periods of the oscillations at the critical value according to the previously determined laws. This table shows that as the aspect ratio increases all the quantities tend, continuously and monotonically, towards the critical values corresponding to the case of an infinite-aspect-ratio cavity.

3.3. *Development of solutions resulting from the instability of the conduction regime*

Solutions were computed for increasing values of the Rayleigh number taking in general one instantaneous solution obtained for an immediately lower value of Ra as the initial condition. Steps of 10^3 in Rayleigh number were generally taken, i.e. solutions were obtained for 9×10^3, 1×10^4, 1.1×10^4. After some initial aperiodic transient consecutive to the sudden change in the value of the Rayleigh number, the solutions quickly resumed a time-periodic behaviour. Their time–space structure showed no qualitative difference with the solutions obtained for 7×10^3 or 8×10^3 apart from an increase of the amplitude of the fluctuations. Figure 4 presents the amplitude of the temperature fluctuations at the monitoring point as a function of the Rayleigh number over the range 6.8×10^3–1.3×10^4. On the same figure the dashed line represents the parabola corresponding to the Hopf bifurcation amplitude curve. Its shape was determined from the linear relationship shown in figure 3 and this curve is tangent to the actual amplification curve at the critical Rayleigh number. Nonlinear effects become sizeable for Ra larger than 8×10^4 and the curve shows that the solution presents fluctuations of almost constant amplitude (independent of the Rayleigh number) in the range 9×10^3–1.1×10^4. The amplitude of the temperature fluctuations has then increased to about 22 % of the temperature difference across the cavity. This results in visible effects on the time–space structure of the solution as shown in figure 5, which presents time sequences of the temperature

A	16	20	25	∞
Ra_c	6850	6185	5965	5770
λ_c	2.07	2.14	2.17	2.24
α_c	6.3×10^{-4}	6.6×10^{-4}	6.7×10^{-4}	7.0×10^{-5}

TABLE 2. Evolution of the critical parameters, $\eta = 0.8$; $A = \infty$ taken from Choi & Korpela

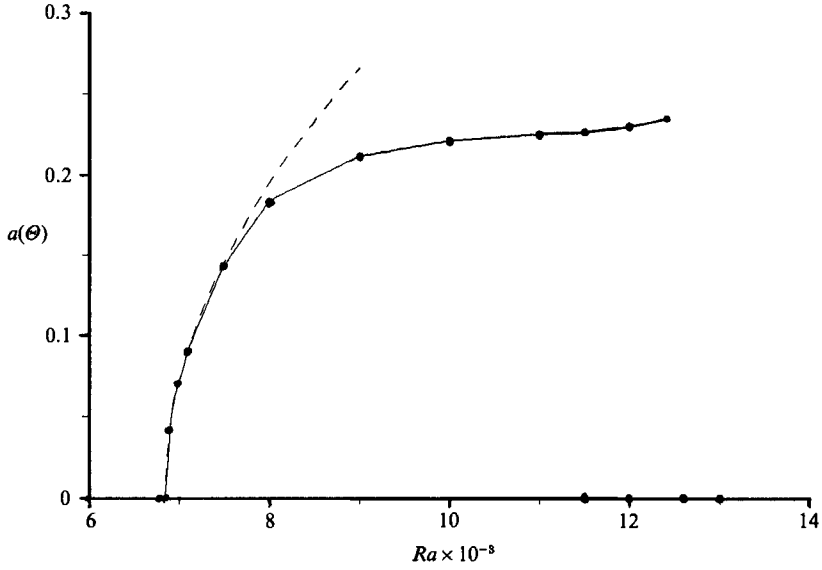

FIGURE 4. Evolution of the amplitude of temperature fluctuation $a(\Theta)$ at the monitoring point $\zeta = 0$, $z = 0.26$ as a function of Ra; $A = 16$, $\eta = 0.8$. Filled circles indicate stable steady ($a(\Theta) = 0$) or unsteady solutions.

and stream-function fields for Ra equal to 1.1×10^4. The isotherms in the middle of the cavity are seen to evolve similarly to a travelling wave and the number of closed rolls varies periodically between 3 and 4. This is in good agreement with the results already obtained by Lee *et al.* (1982) for somewhat different values of the parameters.

When the Rayleigh number is further increased to 1.2×10^4, a qualitative change is observed in the evolution of the time-dependent solution which has undergone a period-doubling (frequency-halving) bifurcation. This is confirmed by the density power spectrum of the temperature signal at the sampling point (figure 6) which shows the presence of the $\frac{1}{2}f$ subharmonic and of several linear combinations $pf+q\frac{1}{2}f$. We have narrowed the range of values in which this subharmonic bifurcation takes place and found it to occur between 1.18×10^4 and 1.19×10^4. The amplitude of this period-doubling bifurcation is very weak and has almost no macroscopic visible effect.

3.4. *Return to steady state – reverse transition*

Solutions showing period-doubling exist for values of the Rayleigh number in the range 1.19×10^4–1.24×10^4. When the Rayleigh number is further increased to 1.26×10^4 starting from an instantaneous solution obtained for 1.24×10^4 as the initial condition, the solution first begins to show large-amplitude oscillations of period approximately equal to 30 time units. After two such oscillations, it then evolves very rapidly back to a steady state which is achieved after 150 time units.

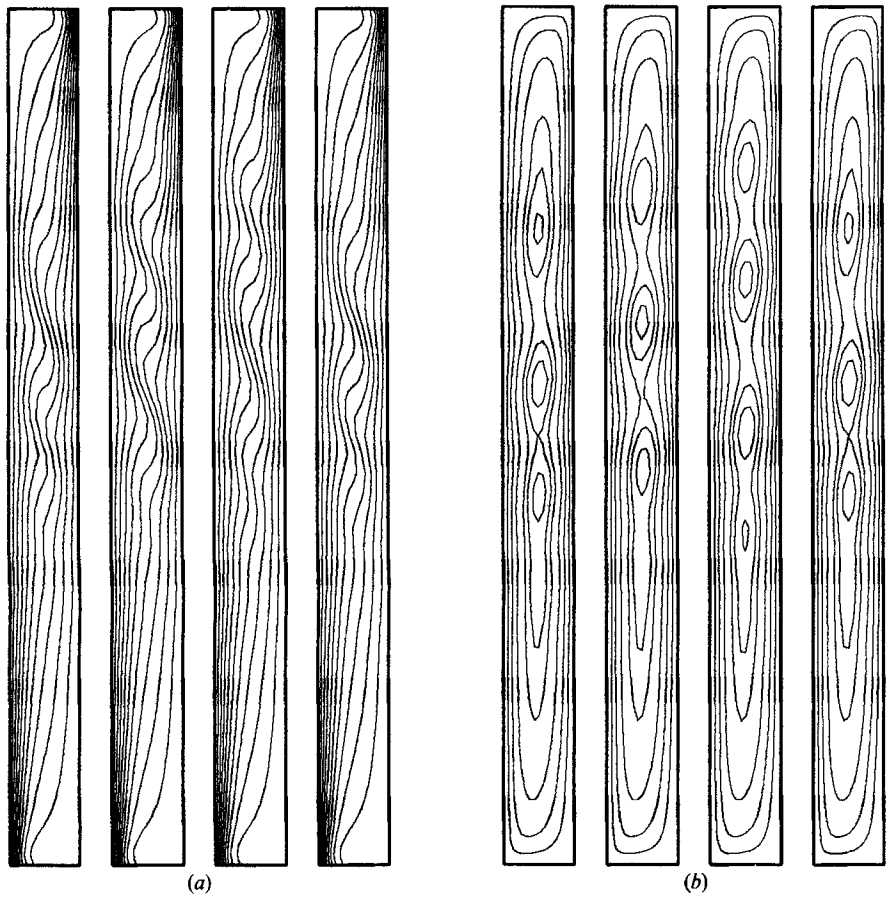

FIGURE 5. Time sequences of the temperature (a) and stream-function (b) fields for $Ra = 1.1 \times 10^4$; $A = 16$, $\eta = 0.8$; $N = 24$, $M = 72$. Time interval is 7.0. Stream-function isovalues are 0.0005, 0.0015, 0.003, 0.005, 0.006, 0.007.

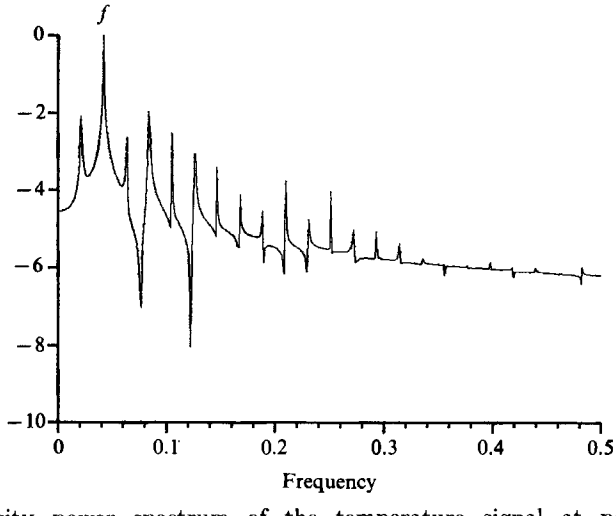

FIGURE 6. Density power spectrum of the temperature signal at point $\zeta = 0$, $z = 0.26$; $Ra = 1.2 \times 10^4$; $A = 16$, $\eta = 0.8$; $N = 24$, $M = 72$; sampling of 2048 points over time interval of 983.04.

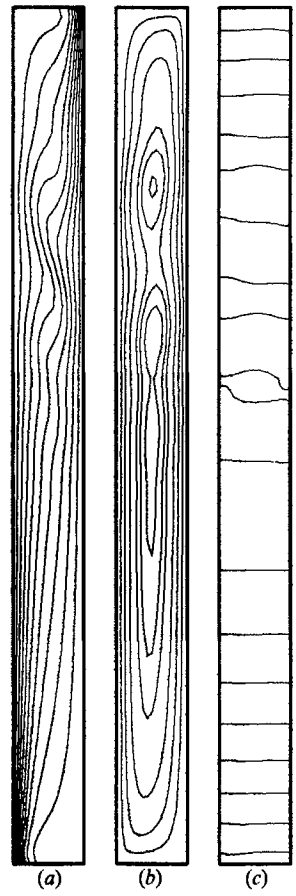

FIGURE 7. Temperature (*a*), stream function (*b*) and pressure field (*c*), $Ra = 1.26 \times 10^4$; $A = 16$, $\eta = 0.8$; $N = 24$, $M = 72$. Stream-function isovalues are 0.0005, 0.0015, 0.003, 0.005, 0.006, 0.007.

Note that the steady solution obtained for Ra equal to 1.26×10^4 is still characteristic of the 'cat's eye' regime as indicated by the presence of closed rolls and by the waviness of the isotherms in the middle part of the cavity (figure 7). This indicates that the reverse transition from unsteady to steady solutions is not directly linked to disappearance of the multicellular flow structure in the core. Another major difference between this steady solution and the unsteady solution displayed on figure 5 for instance, is clearly a reduction of the number of rolls. This steady solution is indeed characterized by two main rolls even though a third extremum is visible on the stream-function pattern.

When the Rayleigh number is decreased quasi-statically, a slight hysteresis is found in the region around 1.2×10^4. Steady-state solutions can be found for Ra values down to 1.15×10^4. These solutions were integrated for very long times and showed no hint of instability. We believe that these solutions are stable steady-state solutions of the Boussinesq equations. When the value of the Rayleigh number is decreased to 1.12×10^4 starting from the solution obtained for 1.15×10^4 as the initial condition, the solution jumps back onto the unsteady time-periodic solution already found in the up-scan as shown in figure 8.

Starting from the steady solution corresponding to 1.26×10^4 as initial condition,

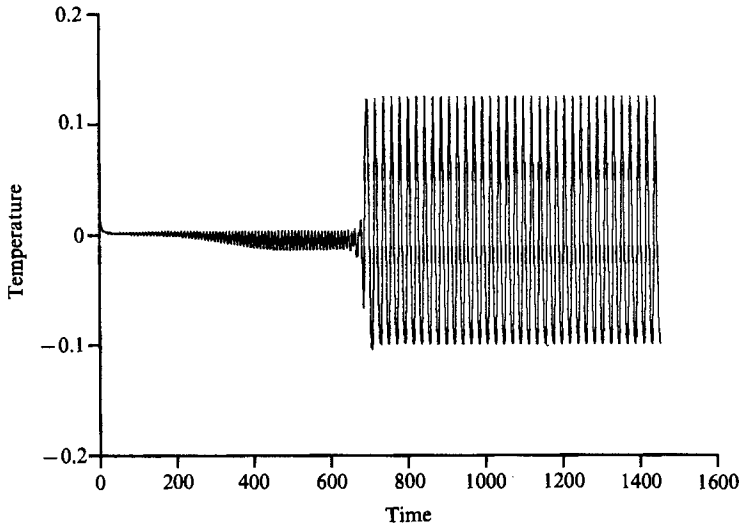

FIGURE 8. Time evolution of the temperature at point $\zeta = 0$, $z = 0.26$; $Ra = 1.12 \times 10^4$; $A = 16$, $\eta = 0.8$; $N = 24$, $M = 72$.

the Ra-value was then sequentially increased to 2×10^4 and 3×10^4. The corresponding asymptotic solutions were found steady. Their streamline and isotherm patterns show that these solutions are now truly characterized by a two-cell structure (figure 9). The Ra-value was then set to 3.2×10^4 and, to our surprise, the asymptotic solution was then found to be time periodic with a dimensionless period of approximately 14. A time sequence of the stream function shows that the unsteadiness corresponds to an oscillation of the roll centres around their mean position. The rolls come closer and move away simultaneously in contrast with the cat's eye unsteadiness which corresponds to an upward drift of the cells. Unsteady solutions displaying similar characteristics were also found for increasing Ra values of 3.4×10^4 and 3.5×10^4. The Ra-value was then further increased to 3.6×10^4 for which the corresponding asymptotic solution was found steady. As evidenced by its streamline and isotherm patterns shown in figure 10, this solution is now characterized by a monocellular flow structure of boundary-layer type with a vertical stratified core region. This monocellular solution was then used as initial condition to integrate the equations with decreasing Ra. Steady monocellular flow solutions were obtained for Ra values down to 1.8×10^4. On this branch of solutions no unsteady solution was found. Integration with Ra set to 1.6×10^4 starting from the solution found for Ra equal to 1.8×10^4 as initial condition, leads to a steady two-cell flow which belongs to the two-cell solution branch already obtained for increasing Ra-values.

These results show that, in the particular cavity investigated here, the solution of the two-dimensional axisymmetric Boussinesq equations undergoes a reverse transition from unsteady multi-cellular to steady monocellular flow structure as the Rayleigh number increases. The conjecture of Roux *et al.* (1980) for cavities in Cartesian coordinates seem thus to apply to annular cavities as well, with the major difference that, in Cartesian cavities, this reverse transition is supposed to take place from steady multicellular to steady monocellular flow. Reverse transitions in the Cartesian case have already been observed in the numerical computations of Roux *et al.* (1980) and of Lauriat & Desrayaud (1985*b*) for instance. In the annular cavity

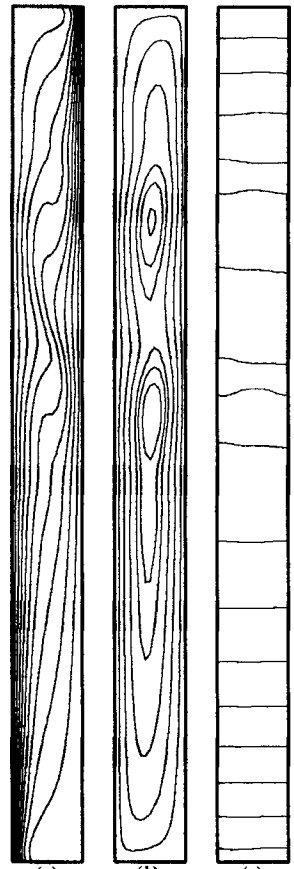

FIGURE 9. Temperature (*a*), stream function (*b*) and pressure field (*c*), $Ra = 2 \times 10^4$; $A = 16$, $\eta = 0.8$; $N = 24$, $M = 72$. Stream-function isovalues are 0.0005, 0.0015, 0.003, 0.005, 0.006, 0.007, 0.008.

investigated here, this reverse transition seems, however, much more complex than anticipated. To summarize, the return from unsteady multicellular flows to steady monocellular flows seems to occur through several distinct steps. There is first a transition from unsteady three-cell flow to a steady two-cell flow around *Ra* equal 1.2×10^4. This two-cell solution becomes unsteady for *Ra*-values approximately equal to 3.2×10^4. A further increase of the *Ra*-value to 3.6×10^4 eventually yields the steady monocellular flow. These changes in the number of cells are characterized by hysterisis. These different transitions are summarized in the diagram shown in figure 11 where the solution branches are classified by their number of cells. The choice may seem somewhat arbitrary in view of the uncertainty in the number of rolls for some of the solutions but it helps classify the different solutions.

These results are somewhat surprising in view of what is known from the Cartesian case, even though no one has really investigated numerically in any detail this reverse transition process which might also prove more complex than expected. Note for instance, that Lauriat & Desrayaud (1985*b*) mention that, for values of the Rayleigh number in the vicinity of the reverse transition, their scheme would not converge when using solutions corresponding to lower *Ra*-values as initial condition

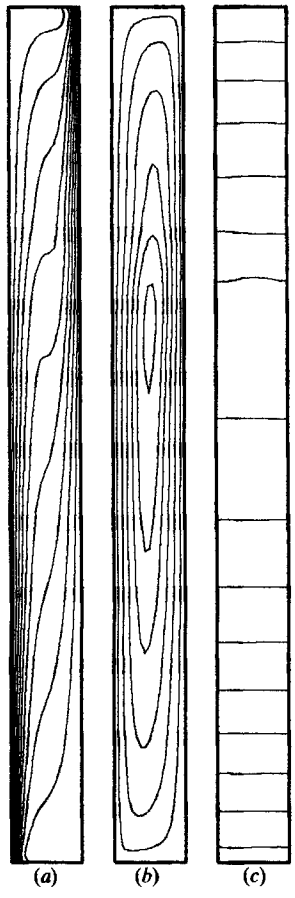

FIGURE 10. Temperature (a), stream function (b) and pressure field (c), $Ra = 3.6 \times 10^4$; $A = 16$, $\eta = 0.8$; $N = 24$, $M = 90$. Stream function isovalues are 0.0005, 0.002, 0.004, 0.006, 0.0075, 0.009.

whereas it would converge when starting from solutions corresponding to higher values of Ra.

This led us to investigate the reverse transition in a Cartesian cavity of aspect ratio 16. Detailed results will be presented elsewhere. Let us just briefly mention here that these new results qualitatively agree with the findings in the annular cavity. The number or rolls decreases step by step from four at criticality to one for an Ra value of 4×10^4. Each roll-number change is characterized by hysteresis. Also unsteady two-cell solutions were found in a range of Ra-values in the vicinity of 3.5×10^4, in complete agreement with the corresponding unsteady solutions found on the two-cell branch in the annular cavity. Hysteresis and multiple solutions thus clearly appear as a characteristic feature of these reverse transitions in the Cartesian or cylindrical cases. This agrees with recent experiments performed by Desrayaud (1987) who observed slight hysteresis effects in Cartesian cavities of aspect ratio 13 and 14.

An important conclusion of these numerical experiments in the annular cavity is that the reverse transition is characterized by hysteresis and that for a given Rayleigh number, multiple solutions which have little in common may be found. For instance, in the vicinity of 1.2×10^4, at least two solutions exist: one is steady. The

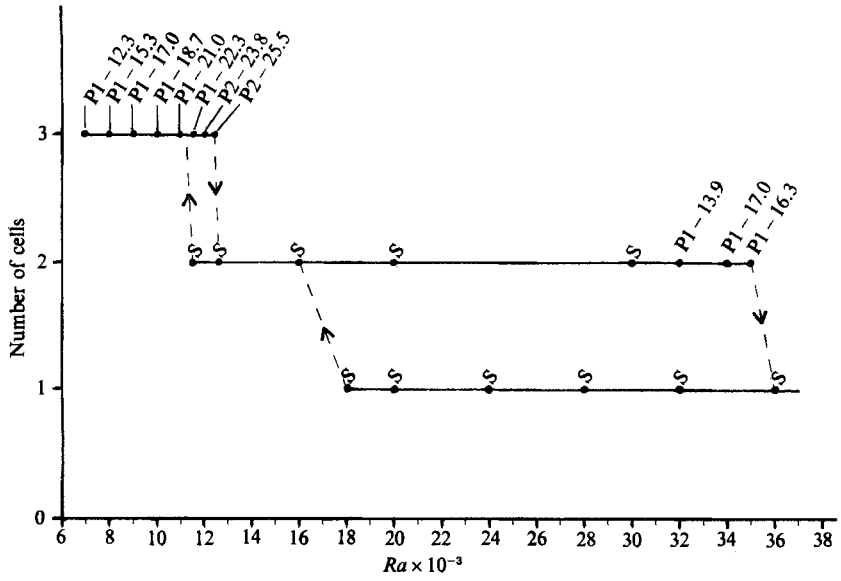

FIGURE 11. Diagram showing the solution branches found for $A = 16$, $\eta = 0.8$. The solutions are labelled S, Steady; P1, time periodic of frequency f; P2, time periodic of fundamental frequency f with subharmonic $\frac{1}{2}f$. The dimensionless oscillation period Π given is $1/f$.

other one is time periodic showing period doubling and presents temperature fluctuations of maximum amplitude on the order of 25% of the temperature difference across the cavity. In these circumstances it is not surprising that the experimental observations seem so contradictory. It would be interesting to study the stability of these two-dimensional steady or unsteady solutions with respect to three-dimensional azimuthal disturbances. This could perhaps help reconcile numerical predictions with experimental observations.

To conclude this section let us mention that reversing the heating, i.e. considering an annulus with cold inner wall and hot outer wall, leads to a downward drift of the cat's eyes.

4. The boundary-layer regime

4.1. *Steady solutions*

As already mentioned in the previous paragraph, a unique steady-state solution was found for values of the Rayleigh number larger than 3.6×10^4. Their streamline and isotherm patterns show that these solutions pertain to the boundary-layer regime. The boundary-layer character of the flow becomes more and more pronounced as the Rayleigh number increases, as can be seen by comparing the solution corresponding to an Ra-value of 2×10^5 (figure 12) with that corresponding to 3.6×10^4 already shown on figure 10. The vertical boundary layers adjacent to the hot and cold wall become thinner and a large vertical stable stratification develops in the core region of the cavity. Another characteristic feature is the inversion of the horizontal temperature gradient in the core region of the cavity which indicates that all the heat is transferred by convection across the cavity. More unexpected are the two dead zones which develop at the top and bottom ends of the cavity. The top one appears first, at a Rayleigh number close to 1×10^5 and both are formed when the Rayleigh

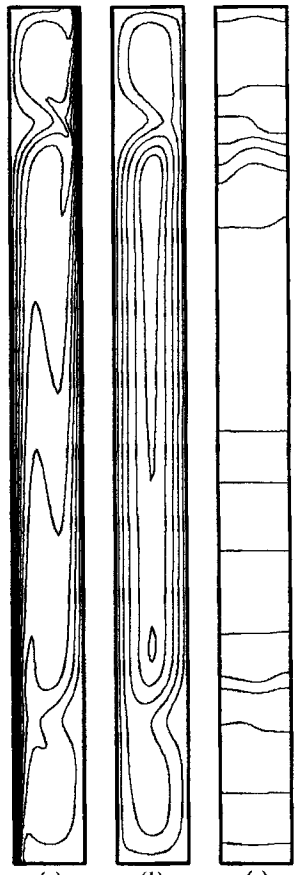

FIGURE 12. Temperature (a), stream function (b) and pressure field (c), $Ra = 2 \times 10^5$; $A = 16$, $\eta = 0.8$; $N = 32$, $M = 161$. Stream-function isovalues are 0.0005, 0.002, 0.004, 0.006, 0.007.

number reaches 2×10^5 (figure 12b). Most of the flow rate bypasses these zones and circulates in a fictitious cavity of smaller aspect ratio than the actual aspect ratio of the cavity. This phenomenon is related to a local thickening of the thermal boundary layer around $z/A = 0.8$ as shown by the isotherms (figure 12a) and is also associated to a strong transverse pressure gradient (figure 12c). The same effect is present, but weaker, along the outer wall. These features were also found by Lauriat & Desrayaud (1985b) in large-aspect-ratio Cartesian cavities. In order to get these solutions we had to dramatically increase the spatial resolution, in particular in the vertical direction: it was found necessary to increase M to 160 and N to 32 to adequately resolve the solution for a value of Ra equal to 2×10^5. It is believed that it is the presence of the region of high vertical shear linked to the detached boundary layer that causes these numerical resolution difficulties. Indeed, this larger vertical gradient is located in the interior of the cavity where the number of Chebyshev polynomials needed to resolve spatial scales or order ϵ varies like ϵ^{-1}, as opposed to $\epsilon^{-\frac{1}{2}}$ when the regions of strong variations are located at the walls. Numerical integration performed with coarser resolutions would predict spurious, very high-frequency oscillating solutions, as is generally the case for spectral methods with insufficient spatial resolutions (see e.g. Orszag & Kells 1980; Marcus 1981; Curry *et al.* 1984).

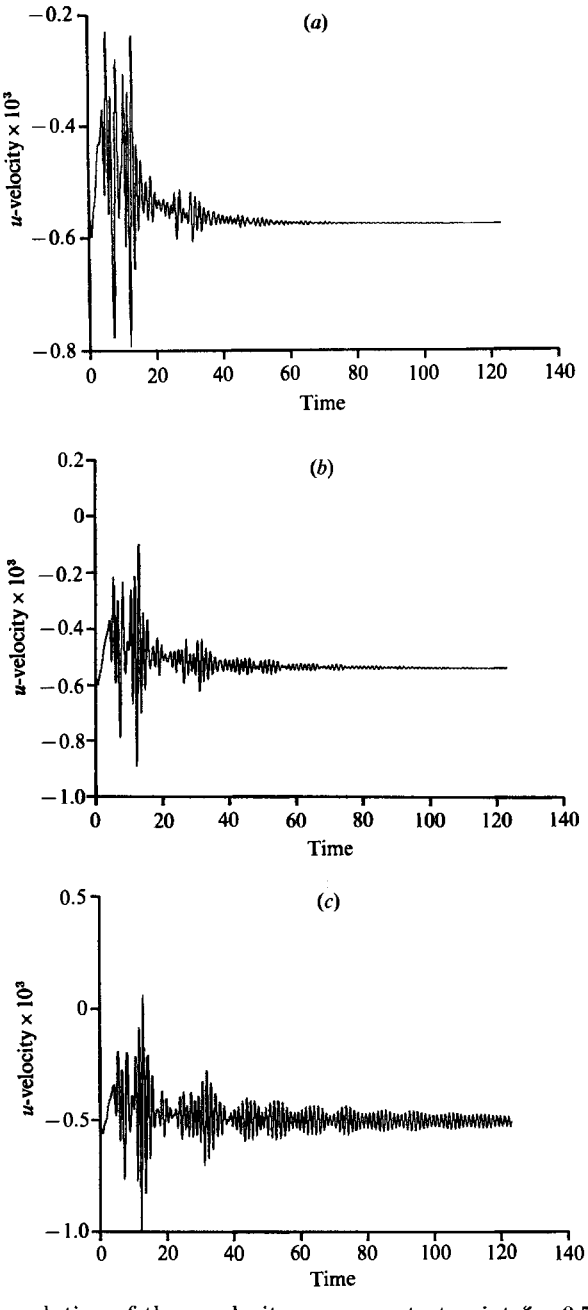

FIGURE 13. Time evolution of the u-velocity component at point $\zeta = 0.71$, $z = -0.26$; (*a*) $Ra = 2.1 \times 10^5$; (*b*) $Ra = 2.2 \times 10^5$; (*c*) $Ra = 2.3 \times 10^5$; $A = 16$, $\eta = 0.8$; $N = 32$, $M = 160$. Time integration carried out with $\Delta t = 0.003$.

Figure 13 presents the time evolution of the u-velocity component at the sampling point for three Rayleigh number values, respectively equal to 2.1, 2.2 and 2.3×10^5. Note that the location of the sampling point has been moved to the bottom of the downward boundary layer where the phenomena are more clearly visible as will be shown later. These time traces show that the three solutions eventually return to a

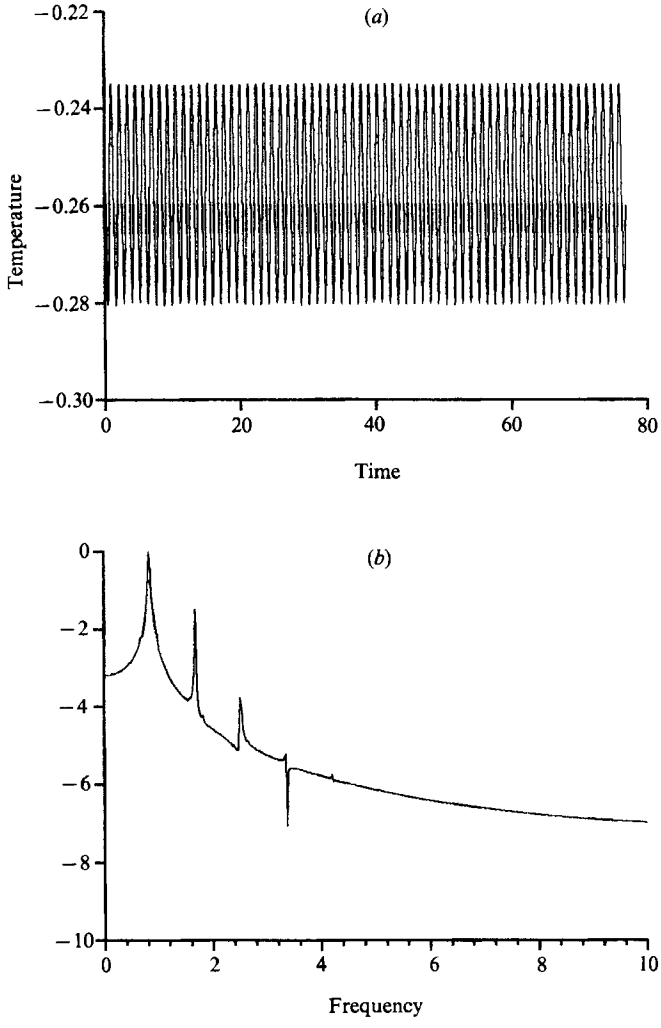

FIGURE 14. (*a*) Time evolution of the temperature at points $\zeta = 0.71$, $z = -0.26$; $Ra = 2.5 \times 10^5$; $A = 16, \eta = 0.8; N = 32, M = 180$. (*b*) Density power spectrum of this signal: sampling of 1024 points over time interval of 40.96.

steady state but the time needed to achieve steady state increases with increasing Rayleigh numbers. These evolutions are qualitatively similar: a high-frequency oscillation is modulated by a low-frequency phenomenon. The high-frequency oscillations correspond to travelling waves in the boundary layers. These waves are excited during the transients and slowly die out as integration time tends toward infinity. The origin of the low-frequency modulation is still not clear at present: it may correspond to a perturbation that is generated when the Rayleigh number is suddenly increased and that is advected by the primary circulation around the cavity, or to some oscillations of internal gravity waves sustained by the stratified core region of the cavity. Patterson (1984) has indeed shown that these internal gravity waves determine the asymptotic behaviour to steady state in cavities of aspect ratio of order 1. These evolutions are very similar to those obtained in a Cartesian cavity of aspect ratio equal to 8 by Le Quéré & Alziary de Roquefort

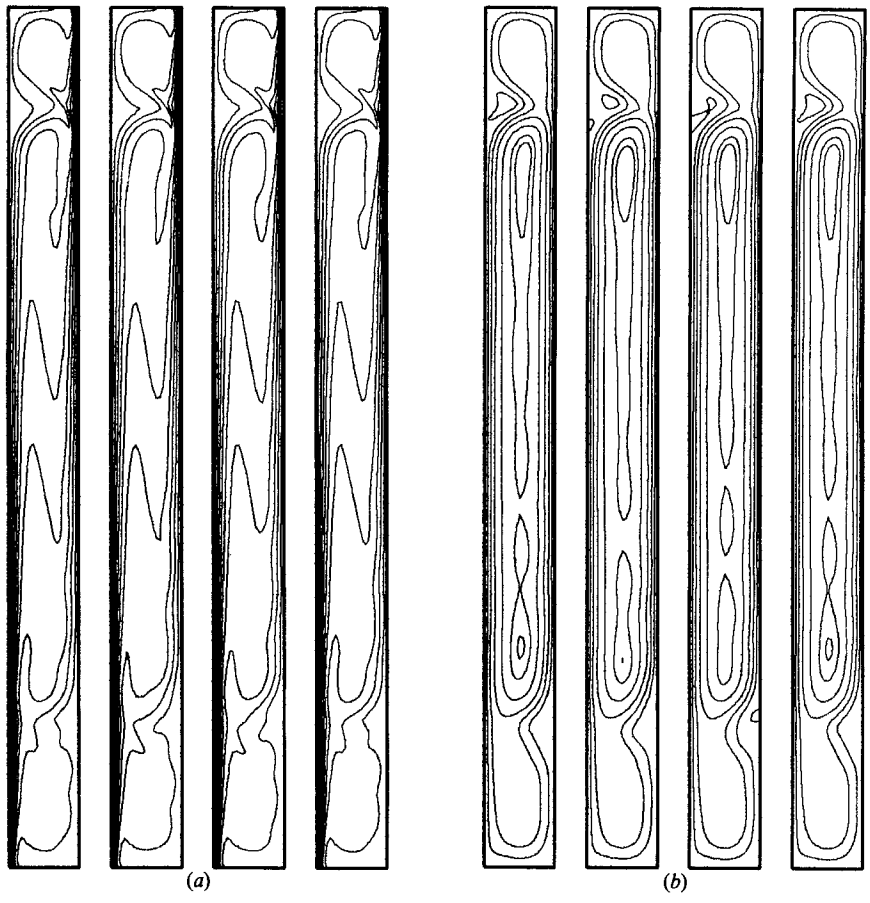

FIGURE 15. Time sequence of temperature field (*a*) and of stream-function field (*b*), $Ra = 2.5 \times 10^5$; $N = 32$, $M = 180$. Time interval is 0.58. Stream-function isovalues are 0, 0.0005, 0.0015, 0.003, 0.005, 0.0065, 0.007.

(1985*b*) and likewise suggest that the boundary-layer flow is close to becoming unsteady.

4.2. *Unsteady boundary-layer regime*

4.2.1. *Structure of the unsteady solution*

When the value of the Rayleigh number is increased to 2.5×10^5, the numerical algorithm gives an asymptotic solution that is unsteady, time periodic and presents fluctuations of constant amplitude (figure 14*a*). The asymptotic solution is achieved after a transient evolution composed of a high-frequency signal modulated by a low-frequency phenomenon. The low-frequency modulation slowly dies out as the integration time tends to infinity which gives a single frequency dependence of the solution as confirmed by the density power spectrum of this signal (figure 14*b*). It should be noted that the maximum amplitude of the temperature fluctuations is on the order of $\pm 2\%$ of the temperature difference across the gap. This indicates that this boundary-layer instability has a weak perturbation growth rate in the vicinity of the critical Rayleigh number. In order to obtain this solution we have to slightly increase the resolution in the vertical direction which is now $M = 180$ (N was kept equal to 32). The time step was taken as 2.5×10^{-3}. Figure 15 presents time sequences

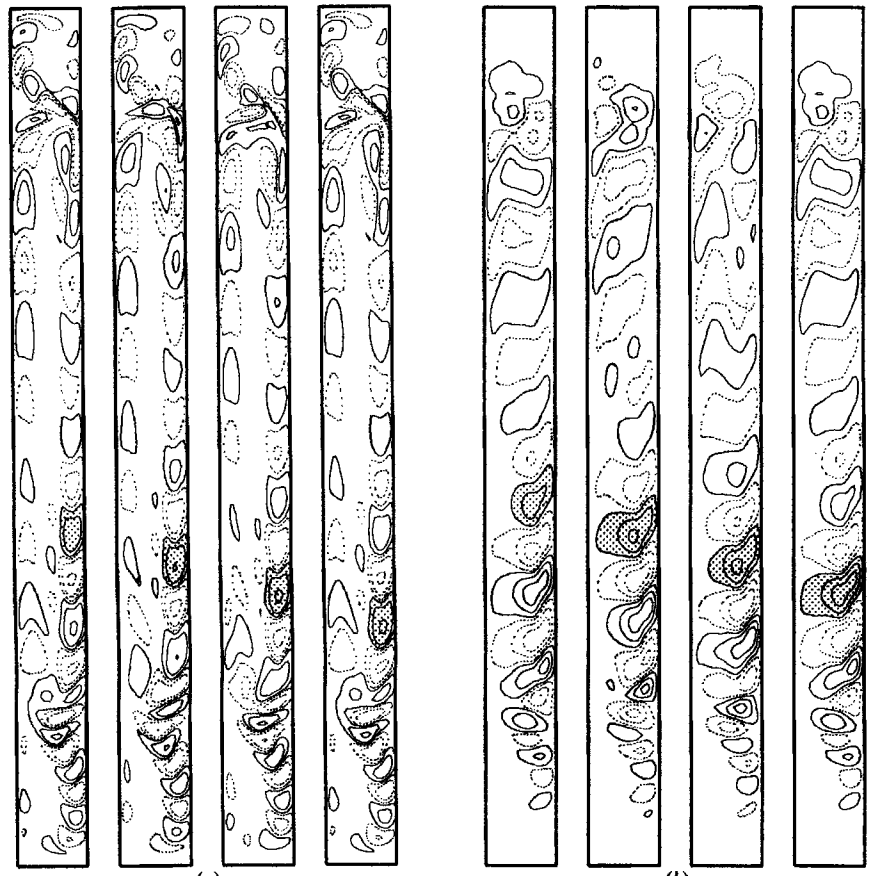

FIGURE 16. Time sequence of fluctuating temperature field (a) and of fluctuating stream-function field (b), $Ra = 2.5 \times 10^5$; $N = 32, M = 180$. Isovalues of fluctuating temperature are ± 0.02, ± 0.008, ± 0.002; isovalues of fluctuating stream function are ± 0.00015, ± 0.00008, ± 0.00002; negative isovalues are shown as dotted lines. One structure is shaded in grey so that its motion can be followed.

of the temperature and stream-function fields over one period of oscillation. Even though the amplitude of the fluctuations is small, waviness of the isotherms is visible just before the boundary layer separates both along the cold and hot walls. The stream-function plots (figure 15b) show a small recirculation zone that appears periodically at the location where the upward boundary layer detaches from the hot wall. Figure 16 presents the corresponding time sequences of the fluctuating temperature and stream-function fields obtained in the manner already described in §3.2. The temperature fluctuations are seen to be confined within the boundary layers. In the middle part of the cavity these fluctuations are of very small amplitude, in sharp contrast with the structures characteristic of a cat's eye instability. In each boundary layer, the temperature fluctuations reach their maximum amplitude in the downstream region just before the flow turns around. Rather surprisingly, the temperature fluctuations are seen to be much larger in the descending boundary layer along the cold outer wall than in the ascending boundary layer along the hot inner wall. They are carried along by the primary circulation and they thus circulate in the fictitious cavity of smaller aspect ratio at a wave speed

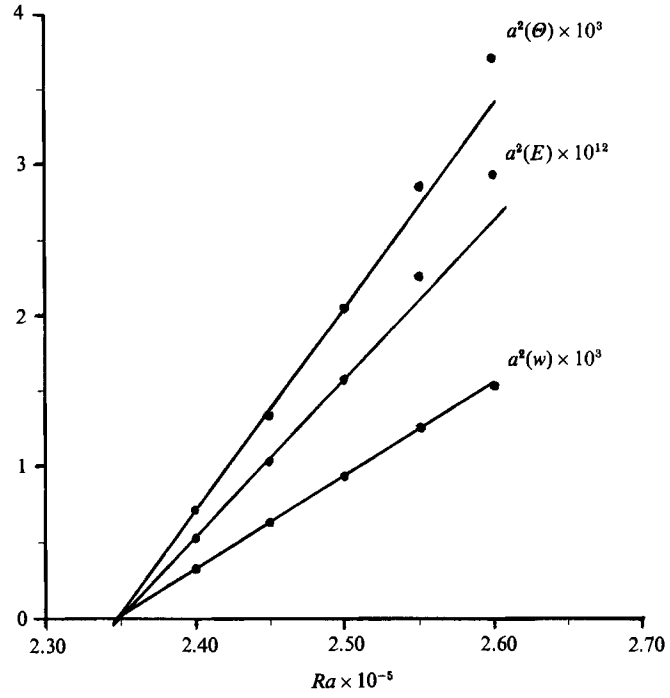

FIGURE 17. Evolution of the squared amplitudes of temperature $a^2(\Theta)$, of the w-velocity component $a^2(w)$ and of $a^2(E)$ as a function of Ra; $A = 16$, $\eta = 0.8$; location of monitoring point: $\zeta = 0.71$, $z = -0.26$.

close to the maximum value of the vertical velocity in the boundary layer. In addition small structures separate in the region of high shear and accumulate in the dead end zones where they pile up at the top and bottom walls and are gradually smeared out. The stream-function fluctuations are seen to extend across the gap and reach their maximum amplitude in the same region as the temperature fluctuations.

4.2.2 *Accurate determination of the critical* Ra_c

It is possible to obtain an accurate estimate of the critical value if one again assumes that the loss of stability is due to a supercritical Hopf bifurcation. Several asymptotic solutions were thus computed in the vicinity of the critical Rayleigh number, i.e. for values of Ra equal to 2.4, 2.45, 2.5, 2.55 and 2.6×10^5. Figure 17 presents the evolution of the squared amplitudes of the fluctuations of the temperature and w-velocity component at the sampling point and of $E(\Theta)$ previously defined. These quantities increase linearly with Ra over this range and extrapolation of these linear relationships to zero amplitude provides an accurate estimate of the critical Rayleigh number equal to 2.35×10^5.

Table 3 presents the period Π of the corresponding solutions In the second column we show the number N of time steps per period. It can be seen that the period Π varies by less than 0.2% when the Rayleigh number increases by almost 8%. Π can thus be considered as independent of Ra over this range. This result shows that the dimensional period of the oscillations varies like $(H/\Delta T)^{0.5}$. This result is consistent with the dependence found in the Cartesian case for the same type of boundary-layer instability (Le Quéré & Alziary de Roquefort 1986). For this type of instability, increasing the temperature difference decreases the dimensional period of the

Ra	N	Π
2.40×10^5	475.2	1.1880
2.45×10^5	475.3	1.1882
2.50×10^5	475.9	1.1897
2.55×10^5	475.8	1.1895
2.60×10^5	475.6	1.1890

TABLE 3. Evolution of the period Π of oscillations; $A = 16$, $\eta = 0.80$

travelling waves. (This result strongly suggests that the surprising dependences found at §3.2.3 concerning the cat's eye instability are not spurious numerical effects since these solutions at low Rayleigh numbers were much easier to compute than those for the high Rayleigh numbers.) Note that a value of Ra equal to 2.5×10^5 based on cavity width corresponds to a Rayleigh number based on cavity height of 1.024×10^9. This value can be achieved with a temperature difference of 10 °K in a cavity which is roughly 1 m tall and 0.06 m wide. The corresponding period of the travelling waves is then about 1.5 s.

5. Local and global Nusselt numbers

The local instantaneous Nusselt numbers is defined as the normal derivative of an instantaneous temperature field at the vertical walls $r = r_1$ and $r = r_2$ respectively:

$$Nu_1(z,t) = \frac{\partial \Theta}{\partial r}(r = r_1, z, t),$$

$$Nu_2(z,t) = \frac{\partial \Theta}{\partial r}(r = r_2, z, t).$$

For steady solutions these definitions reduce to the classical ones. The mean space values at the walls are then defined as

$$\overline{Nu_1}(t) = \frac{1}{2}\int_{-1}^{1} \frac{\partial \Theta}{\partial r}(r = r_1, z, t)\,\mathrm{d}z,$$

$$\overline{Nu_2}(t) = \frac{1}{2}\int_{-1}^{1} \frac{\partial \Theta}{\partial r}(r = r_2, z, t)\,\mathrm{d}z.$$

Note that both the local and mean space value can be obtained with spectral accuracy. The mean time–space value is obtained from an arithmetic mean of the mean space value over a time period of the oscillation. We also define two local curves which are respectively the upper and lower envelopes in time of the local instantaneous Nusselt number

$$Nu_{\max}(z) = \max_{t_0 \leqslant t \leqslant t_0 + \Pi} Nu(z,t),$$

$$Nu_{\min}(z) = \min_{t_0 \leqslant t \leqslant t_0 + \Pi} Nu(z,t),$$

where t_0 is some arbitrary reference time once the asymptotic solution is reached. $Nu_{\max}(z) - Nu_{\min}(z)$ measures the amplitude of the fluctuations of the local Nusselt number at a given elevation z.

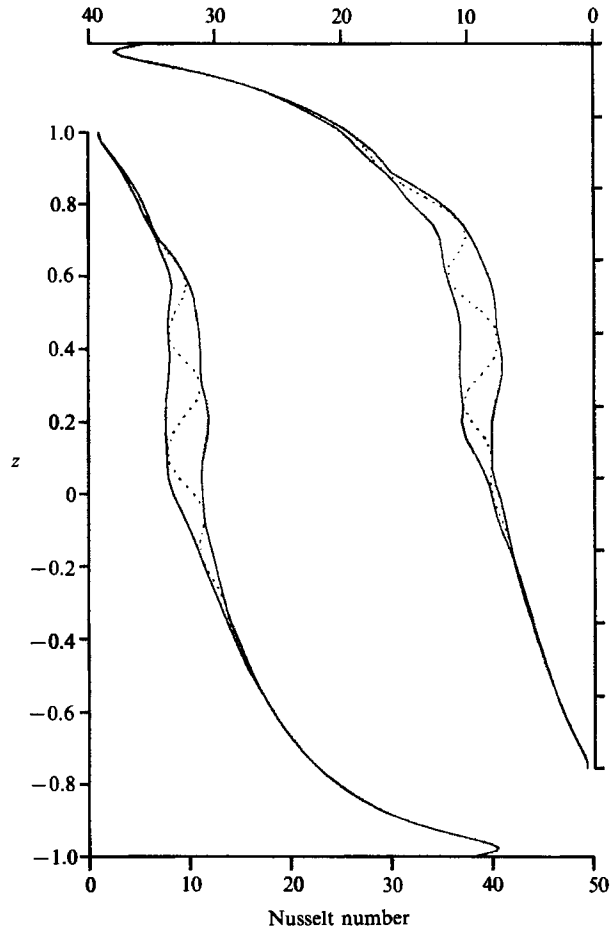

FIGURE 18. Local Nusselt numbers along the inner (left) and outer (right) walls, $Ra = 1.0 \times 10^4$; $A = 16$, $\eta = 0.8$. The solid lines are $Nu_{\max}(z)$ and $Nu_{\min}(z)$. The dotted line is a typical instantaneous $Nu(z,t)$-distribution.

5.1. *Conduction regime*

In the steady conduction regime, the isotherms are parallel to the vertical walls. Heat transfer is mainly due to conduction and the local Nusselt numbers remain almost constant over the central part of the cavity. The appearance of the unsteady conduction regime results in unsteady local and mean-space Nusselt numbers. Figure 18 presents local Nusselt-number distributions along the inner and outer walls for a value of Ra equal to 1×10^4. The solid lines correspond to $Nu_{\max}$ and $Nu_{\min}$; a typical instantaneous local Nusselt number distribution is shown by the dotted line. Its waviness reflects the presence of the cat's eyes in the flow and it evolves in time like a travelling wave propagating upwards. This particular solution is characterized by a maximum amplitude in the temperature fluctuations approximately equal to 22%. As a consequence, the local Nusselt number shows rather large-amplitude fluctuations since the relative difference $(Nu_{\max} - Nu_{\min})/0.5(Nu_{\max} + Nu_{\min})$ reaches a maximum on the order of 30%. This maximum amplitude is found just above midheight of the cavity in agreement with the structure of the unsteady solution.

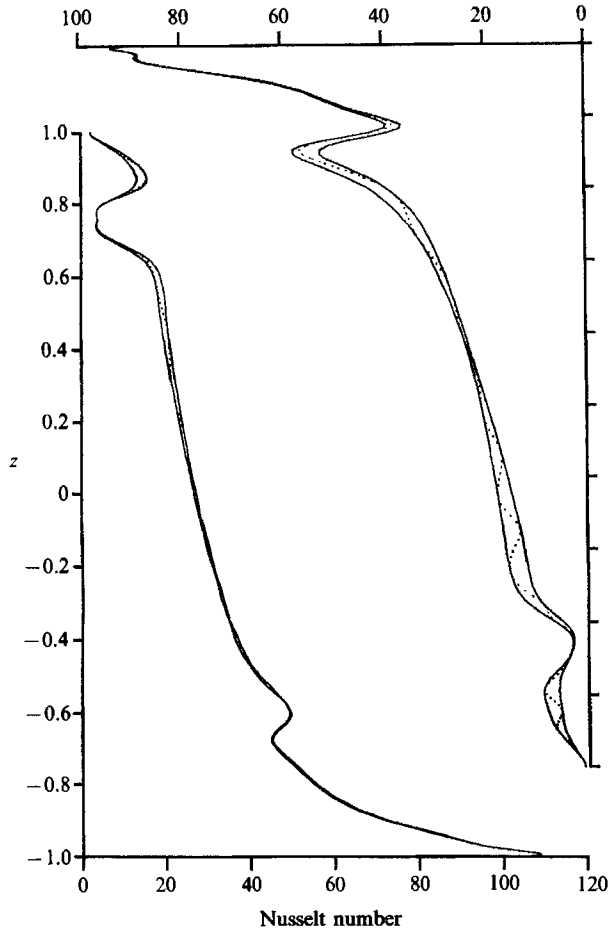

FIGURE 19. Local Nusselt numbers along the inner (left) and outer (right) walls, $Ra = 2.5 \times 10^5$; $A = 16$, $\eta = 0.8$. The solid lines are $Nu_{\max}(z)$ and $Nu_{\min}(z)$. The dotted line is a typical instantaneous $Nu(z, t)$-distribution.

5.2. *Boundary-layer regime*

5.2.1. *Steady boundary-layer regime*

When the solutions enter the boundary-layer regime the local Nusselt-number distributions take the usual characteristic shape found in Cartesian cavities. Its value is maximum in the starting corner of the boundary layer and decreases sharply downstream of this point. The formation of the dead end zones qualitatively alters the shape of these distributions. Local thickening of the thermal boundary layer at the location where the flow turns around causes a sharp local decrease in Nusselt number. This results in large local gradients of these local Nusselt-number distributions.

5.2.2. *Unsteady boundary-layer regime*

Figure 19 presents various local Nusselt-number distributions for the unsteady solution corresponding to an Ra-value of 2.5×10^5 discussed in §4.2.1. On the figure are plotted $Nu_{\max}$, $Nu_{\min}$ and a typical instantaneous Nusselt-number distribution with the same notation as that used in figure 18. Their overall shapes are

characteristic of the boundary-layer regime and display the region of strong variation described in the previous subsection. The waviness of the instantaneous Nusselt-number distribution reflects the travelling wave structure of the boundary layer. The amplitude of fluctuations of the local Nusselt number is thus larger along the outer wall than along the inner wall, as was found for the fluctuating temperature field. This maximum amplitude is reached in the downstream part of the downward boundary layer.

5.3. *Global Nusselt number*

The amplitude of the fluctuations of $\overline{Nu_1}$ and $\overline{Nu_2}$ for both types of unsteady motion remain small even though the local fluctuations may be quite large. This is due to a combination of two factors: the local Nusselt-number distributions take the form of travelling waves and the local fluctuations reach their maximum amplitude in regions corresponding to small absolute values of the local Nusselt number.

The cylindrical nature of the configuration and the adiabatic boundary conditions imposed on the top and bottom walls imply that, at least for steady solutions, $r_1\overline{Nu_1} = r_2\overline{Nu_2}$. All global Nusselt numbers obtained for values of the Rayleigh numbers in the range 4×10^3–2.5×10^5 may be correlated with a good accuracy by $rNu = 1.035Ra^{0.275}$. Note that these values are based on H as reference length and should be divided by $\frac{1}{2}A$ (i.e. 8) in order to be compared to more conventional values based on $(r_2 - r_1)$ as reference length.

6. Conclusion

Axisymmetric natural convection of air in a tall vertical differentially heated annulus has been investigated numerically with a Chebyshev spectral method. In particular, the different flow transitions were carefully studied in a cavity of aspect ratio 16 and radius ratio $\eta = 0.8$. In the range of values investigated, several distinct transitions were found when increasing Ra. Two of them correspond to a steady–unsteady transition while a third one is a reverse (unsteady–steady) transition. The first instability leading to unsteady motion takes place at low values of the Rayleigh number (6850 for $A = 16$, $\eta = 0.8$) when the flow pertains to the conduction regime. This instability takes the form of unsteady cross-rolls (cat's eyes) drifting slowly upwards when the inner cylinder is heated and downwards when the outer cylinder is heated. The second one occurs at much higher values of the Rayleigh number (2.35×10^5 for $A = 16$, $\eta = 0.8$) when the flow is in the boundary-layer regime. This instability takes the form of travelling waves confined within the boundary layers. These two instabilities possess the characteristic features of a supercritical Hopf bifurcation. This has been used to accurately determine the values of the Rayleigh number at which both bifurcations take place. The dimensional oscillation period of travelling wave instability behaves like $(H/\Delta T)^{0.5}$, in agreement with previous results obtained in a Cartesian geometry. The dimensional oscillation periods for the 'cat's eye' instability were found to increase with ΔT in the vicinity of the critical Rayleigh numbers for the three aspect ratio values investigated. Thus, between these two steady–unsteady bifurcations there exists a reverse transition from the unsteady multicellular flow corresponding to the cat's eyes instability to a steady monocellular flow corresponding to the boundary-layer regime. This reverse transition occurs in different steps. There is first an unsteady–steady transition which is accompanied by a reduction in the number of cross-rolls from three to two at values of Ra around 1.2×10^4. The transition to a monocellular structure occurs later, at an Ra-value of 3.6×10^4 approximately. Both transitions exhibit hysterisis

showing that, at a given Rayleigh number, multiple steady or unsteady solutions can be found. Three-cell solutions showing period doubling as well as two-cell unsteady solutions were also found. Investigation of the stability of these axisymmetric solutions with respect to three-dimensional azimuthal disturbances will be the subject of future research.

Computational facilities were provided thanks to the Scientific Committee of the C.C.V.R. which is gratefully acknowledged.

REFERENCES

Bergholz, R. F. 1978 *J. Fluid Mech.* **84**, 743–768.

Choi, I. G. & Korpela, S. A. 1980 *J. Fluid Mech.* **99**, 725–738.

Curry, J. H., Herring, J. R., Loncaric, J. & Orszag, S. A. 1984 *J. Fluid Mech.* **147**, 1–38.

Desrayaud, G. 1987 Thèse d'Etat, University Paris VI.

Ehrenstein, U. 1986 Thesis, University of Nice.

Gottlieb, D. & Orszag, S. A. 1977 *SIAM-CBMS Monograph* 26.

Haidvogel, D. B. & Zang, T. A. 1979 *J. Comput. Phys.* **30**, 167–180.

Haldenwang, P. 1984 Thèse d'Etat, University of Provence.

Hart, J. E. 1971 *J. Fluid Mech.* **47**, 547–576.

Iooss, G. 1972 *Arch. Rat. Mech. Anal.* **47**, 301–320.

Kleiser, L. & Schumann, U. 1980 In *Proc. 3rd GAMM Conf. Num. Methods Fluid Mech.* (ed. E. H. Hirschel), pp. 167–173. Vieweg.

Lauriat, G. & Desrayaud, G. 1985*a* *Int. J. Heat Mass Transfer* **28**, 1613–1617.

Lauriat, G. & Desrayaud, G. 1985*b* *ASME paper* 85-HT-37.

Lee, Y. & Korpela, S. A. 1983 *J. Fluid Mech.* **126**, 91–121.

Lee, Y., Korpela, S. A. & Horne, R. 1982 In *7th Intl Heat Transf. Conf., Munich*, vol. 2, pp. 221–226. Hemisphere.

Le Quéré, P. & Alziary de Roquefort, T. 1982 *C.R. Acad. Sci. Paris* **294**, Serie II, 941–944.

Le Quéré, P. & Alziary de Roquefort, T. 1985*a* *J. Comput. Phys.*, **57**, 210–228.

Le Quéré, P. & Alziary de Roquefort, T. 1985*b* In *Numerical Methods in Laminar and Turbulent Flow*, pp. 841–852. Pineridge.

Le Quéré, P. & Alziary de Roquefort, T. 1986 In *Significant questions in buoyancy affected enclosure or cavity flows, ASME, HTD*, vol. 60, pp. 29–36.

Lin, D. S. & Nansteel, M. W. 1987 *Trans. ASME* C: *J. Heat Transfer* **109**, 899–905.

Marcus, P. S. 1981 *J. Fluid Mech.* **103**, 241–255.

McFadden, G. B., Coriell, S. R., Boisvert, R. F. & Glicksman, M. E. 1984 *Phys. Fluids* **27**, 1359–1361.

Orszag, S. A. & Kells, L. C. 1980 *J. Fluid Mech.* **96**, 159–205.

Patterson, J. C. 1984 *Trans. ASME* C: *J. Heat Transfer* **106**, 104–108.

Prasad, V. & Kulacki, F. A. 1985 *Trans. ASME* C: *J. Heat Transfer* **107**, 596–602.

Roux, B., Grondin, J. C., Bontoux, P. & Vahl Davis, G. de 1980 *Physico Chemical Hydrodyn.* **3**, 292–298.

Shaaban, A. H. & Ozisik, M. N. 1982 In *7th Intl Heat Transf. Conf., Munich*, vol. 2, pp. 281–286. Hemisphere.

Thomas, R. W. & Vahl Davis, G. de 1970 In *4th Intl Heat Transf. Conf., Paris, vol.* 4, paper NC 2.4. Elsevier.

Vahl Davis, G. de & Thomas, R. W. 1969 *Phys. Fluids*, **12**, *suppl II*, 198–207.

Vanel, J. M., Peyret, R. & Bontoux, P. 1986 In *Numerical Methods for Fluid Dynamics II* (ed. K. W. Morton & M. J. Baines) pp. 463–475. Clarendon.

Weidman, P. D. & Mehrdadtehranfar, G. 1985 *Phys. Fluids* **28**, 776–787.